Performance comparison of capping layer materials for double spin-torque magnetic tunnel junctions

Shela Aboud
Synopsys, Inc.
Mountain View, United States
sjaboud@synopsys.com

Julian Schneider
Synopsys Denmark
Copenhagen, Denmark
julians@synopsys.com

Jan-Niclas Luy
Synopsys Denmark
Copenhagen, Denmark
jluy@synopsys.com

Troels Markussen
Synopsys Denmark
Copenhagen, Denmark
troels@synopsys.com

Abstract—We present a computational study of different capping layer materials in double spin-torque MTJ structures. Using fully atomistic calculations based on density functional theory, we calculate key parameters relevant for the read, write, and storage performance of STT-MRAM devices. Among the three candidate materials, Tungsten (W), Tantalum (Ta), and MgO, W is identified as best material for both thermal stability, STT, and TMR, but a very large Gilbert damping can be problematic for reducing the switching current.

Index Terms—STT-MRAM, spin transfer torque, TMR, DFT, Machine-learned force fields, atomistic spin dynamics

I. INTRODUCTION

Spin transfer torque magnetic random access memory (STT-MRAM) is currently being used as standalone and embedded MRAM in modern technology nodes. Further enhancement of the application of STT-MRAM as last level cache requires optimization of the performance and scalability of the magnetic tunnel junction (MTJ) stacks comprising the reference and free magnetic layers as well as additional tunnel barrier and capping layers. In particular, one of the main challenges for further use of STT-MRAM is to reduce the switching current [1]. In order to do so, various MTJ designs are being investigated both in terms of dimensions and novel material compositions [2], [3].

The MTJs used in STT-MRAMs consist of multiple layers of different materials, often with layer thickness below 1 nm, i.e. only a few atomic layers. The free layer (FL) is typically sandwiched between two MgO layers in order to increase the magnetic stability coming mainly from the FeCo-MgO interface. While the traditional STT-MRAM design consists of a single reference layer (RL-1) and a FL, it has recently been proposed to add a second reference layer with fixed magnetization (RL-2), in order to increase the STT efficiency and thus reduce the switching current since contributions from RL-1 and RL-2 are added [2]. This idea was first implemented using a second MgO as capping layer (CL) between the FL and RL-2 forming a double MTJ (DMTJ) [2], which leads to increased STT efficiency, but at the cost of reduced tunneling magneto resistance (TMR), thus compromising the read-operation. More recently, this problem was addressed by using a different (not specified) CL material between the FL and RL-2 forming a double spin-torque MTJ (DS-MTJ) leading to increased STT without sacrificing TMR [3], [4].

In order to explore the large space of potential MTJ designs for improved STT-MRAM performance, accurate and predictable simulations are highly desired. While micromagnetic simulations are often used to simulate the magnetic properties and switching dynamics of STT-MRAM junctions, it relies on a continuum description and requires specified material properties. Given the atomically thin layer sizes, multiple interfaces which significantly alter the bulk properties, as well as the introduction of novel materials, micromagnetic simulations have several shortcomings. A promising alternative is to use fully atomistic simulations which by construction includes the atomic nature of the MTJ stacks. By using first-principles density functional theory (DFT) it is possible to include quantum confinement and interface effects at a rigorous and predictive level. In this paper we demonstrate the capabilities of atomistic modeling of STT-MRAM design by investigating three different CL materials (MgO, W, and Ta) for DMTJ and DS-MTJ structures. We address the main properties relevant for the STT-MRAM performance, namely (i) TMR for reading efficiency, (ii) STT and Gilbert damping for write current reduction, and (iii) thermal stability from atomistic spin dynamics simulations at finite temperatures. Both W and Ta DS-MTJ structures show greatly improved TMR as compared to the DMTJ while still having improved STT as compared to the single MTJ, but the large Gilbert damping for Ta and especially W can be problematic for reducing the switching current.

II. METHODS

All electronic and magnetic properties discussed below are calculated using DFT as implemented in QuantumATK [5]. We expand the wave functions in linear combination of atomic orbitals (LCAO) basis set, which are computationally efficient and allows for non-equilibrium Green's function (NEGF) calculations of currents and torques in device structures. General details of the methods are given in [6].

The multi-layer structures considered in this work are initially set up using a dedicated MRAM builder

tool. The structures are subsequently relaxed with a machine-learned force field of the moment tensor potential (MTP) type [7] specifically trained to Fe, Co, MgO, Ta, and W structures. The results of the structure optimizations are essentially the same as when done with DFT, but can be performed at a fraction of the time. After structure optimization, we form device structures as shown in Fig. 1. We consider structures of the type

Fig. 2. In-plane STT (a) and TMR vs bias voltage (b). The results for the DMTJ (2xMgO) and DS-MTJ (W, Ta) are compared with the result of a single MgO structure (1xMgO)
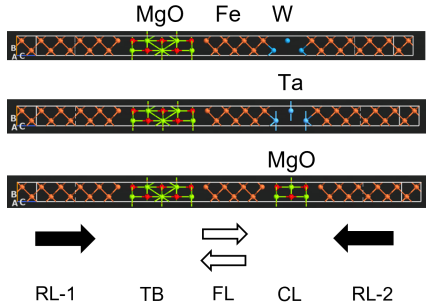

Fig. 1. Three different structures considered. The structures consists of a first reference layer (RL-1), a MgO tunnel barrier (TB), the free layer (FL), a capping layer (CL), and a second reference layer (RL-2). The arrows indicate the magnetization direction in the reference- and free layers.

Fe|MgO(5L)|Fe(7L)|X(3L)|Fe, where (nL) indicates n atomic layers. The first Fe layer is the main reference layer (RL-1) which has a fixed magnetization. This is followed by the MgO tunnel barrier (TB) and the free layer (FL) consisting of 7 Fe atomic layers. The free layer is capped by three layers, X(3), of either MgO, W, or Ta. Finally to the right there is a second reference layer (RL-2), which has opposite magnetization of RL-1.

III. DFT-NEGF FOR STT AND TMR CALCULATIONS

Given the device structures shown in Fig. 1, we calculate both STT and TMR using DFT-NEGF. We speed up the finite-bias calculations significantly by not performing fully self-consistent calculations, but rater impose a linear potential drop across the MgO(5L) layer. In doing so, we only calculate self-consistently the Hamiltonian for the zero-bias configuration. Subsequently we modify the Hamiltonian at each bias point by adding a linear potential drop. For the STT calculation, we additionally update the density matrix. This approximate workflow typically speeds up the calculations by a factor of ~50x. We have verified at a few bias points that the linear potential drop model agrees well with fully self-consistent results.

The STT is calculated as described in [8]. Although we calculate both in-plane and out-of-plane torque components, we here focus on the in-plane components. A full analysis of the out-of-plane components will be presented elsewhere. Fig. 2(a) shows the total in-plane STT component summed over atoms in the free layer as a function of bias voltage for an angle of $\theta = 90°$ between the FL and RL magnetizations. In addition to results for the structures shown in Fig. 1, we also include as reference the results for a Fe|MgO(5L)|Fe structure, i.e. only a single MgO and no capping layer.
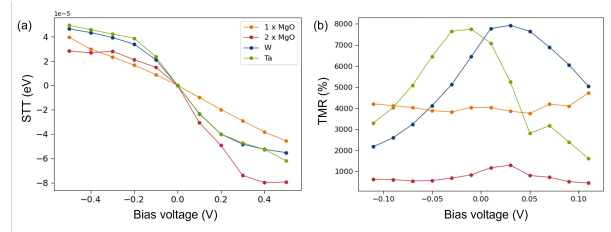
As expected, the DMTJ (2 x MgO) and DS-MTJ (W, Ta) structures gives (numerically) larger STT values due to the contribution from both RL-1 and RL-2. It is however worth noting that the improvement over the single MgO structure is largest for small voltages. At larger voltages a significant non-linearity is observed for the structures with a capping layer.

The TMR is calculated as

$$\text{TMR}(V) = \frac{R_{AP}(V) - R_P(V)}{R_P(V)} \qquad (1)$$

where $R_{P,AP}(V) = V/I_{P,AP}(V)$. The parallel (P)/anti-parallel (AP) configuration is the one where the free layer magnetization is parallel/ anti-parallel to the magnetization in RL-1. Fig. 2(b) shows the TMR calculated for the three structures with capping layer as well as the single-MgO structure. Comparing the single and double MgO structures, we observe a significant decrease in the TMR for MgO-capped DMTJ structure. This finding agrees qualitatively with experimental observations. The W and Ta capped structure behave very differently, however. For those, we observe an increased TMR as compared to the single-MgO structure, at least for small bias voltages.

The TMR and STT results shown above do not include effects of finite temperature, except for the thermal broadening of the Fermi-Dirac distribution functions. It has been experimentally demonstrated that the TMR is reduced by roughly a factor of two when increasing the temperature from 0 K to 300 K [9], [10]. By using a special thermal displacement method [11], [12] it is possible to include the effects of electron-phonon coupling at finite temperatures, provided that the vibrational modes (phonons) of the system can be calculated. Since we have an accurate MTP available, we can very efficiently calculate the phonons and generate the special thermal displacements. In doing so, we get a slightly different configuration at each temperature, for each of which we can calculate the TMR as described above.

Figure 3 shows the relative change of TMR for a single-MgO type structure. In order to more directly compare with experiments from [9] and [10], the MgO consists of 11 atomic layers with a length of approximately 2.1 nm. It is encouraging to see that the relative decrease in TMR as a function of temperature observed in the experiments is well captured by the calculations. A detailed analysis of the temperature-dependence of
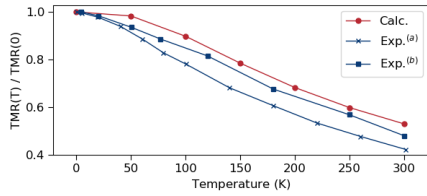
Fig. 3. Relative change of TMR as a function of temperature. Calculated data obtained with QuantumATK is compared with experimental results from [9] (a) and [10] (b).

different capping layers as well as the effect on the STT will be presented elsewhere.

IV. THERMAL STABILITY

We also study the thermal stability of the magnetism in the free layer. For these calculations we do not include the reference layers.

A. Exchange interactions and uniaxial anisotropy constants from DFT

The considered structures are indicated in Fig. 4 (a)-(c) showing the atom-resolved uniaxial magnetocrystalline anisotropy energy (MAE), which we calculate using the magnetic force theorem [13]. From Fig. 4 (a), we recover the well-known result that the MAE is strongly enhanced at the Fe atoms bonding to the oxygen atoms in MgO, whereas the bulk Fe atoms has little MAE. At the right interface to the capping layer (MgO, W, Ta) significant differences are seen for the MAE. Even though W and Ta are next to each other in the periodic table, their effect on the MAE are clearly different: while W leads to an enhanced MAE, Ta reduces it.

In addition to the MAE, we also calculate the Heisenberg exchange interactions J_{ij} from DFT. The implementation in QuantumATK follows [14].

B. Atomistic spin dynamics

Using the uniaxial anisotropy energies and the Heisenberg coupling parameters J_{ij}, we perform atomistic spin dynamics simulations at finite temperatures using the Vampire code [15], [16]. We have developed a fully integrated workflow in QuantumATK to perform Vampire simulation with DFT-calculated parameters, including a graphical user interface for setting up Vampire simulations using DFT input parameters, and dedicated analysis tools for visualization of the results.

Fig. 4 (e) shows the anisotropy energy ΔE for the 10 nm diameter cylindrical shaped structures as shown in panel (d). We note that the Ta capped structure continues to have the lowest ΔE at all temperatures due to the lower uniaxial MAE as seen in (c). The stability factor $\Delta = \frac{\Delta E}{k_B T}$ obtained at 300 K is $\Delta = 23.2, 30.6, 9.3$ for MgO, W, and Ta cappings, respectively. In order to have a stability factor of 60, which is often the target value, the minimum diameter would need to increased to $D_{min} = 16, 14, 25$ nm respectively, assuming that ΔE is proportional to the area. We do note that demagnetization energies have not been included in these

estimates. Doing so would lower ΔE and increase the required diameters.
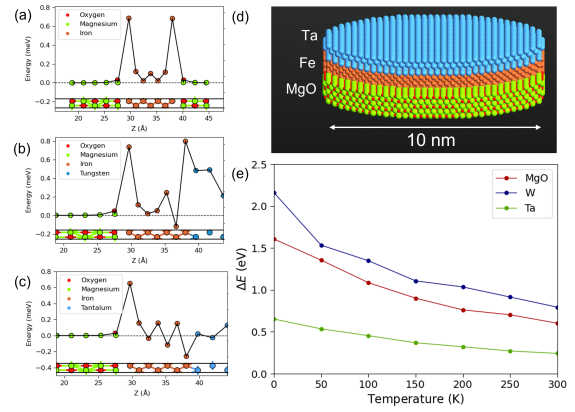

Fig. 4. Atom-resolved anisotropy energies for the three different structures (a)-(c). Panel (d) shows the atomic structure used in Vampire for a 10 nm diameter cylinder. Panel (e) shows the anisotropy energy ΔE vs. temperature for 10 nm diameter cylinders.

In addition to the ΔE calculations we have also calculated the relative magnetization for higher temperatures in order to determine the Curie temperatures. By fitting the magnetization as a function of temperature to the formula $M(T) = (1 - T/T_C)^{\beta}$, we obtain the Curie temperature T_C. The fitted Curie temperatures are 928 K, 1026 K, and 966 K for MgO, W, and Ta cappings, respectively. Although the W-capped structure has a larger Curie temperature, the differences in T_C between the structures does not seem very significant at the relevant application temperature range of 300–400 K.

C. Gilbert damping

The last quantity we calculate is the Gilbert damping constant α. The Gilbert damping tensor is calculated using Kambersky's torque-torque correlation model [17]. Fig. 5 shows the calculated damping constants as a
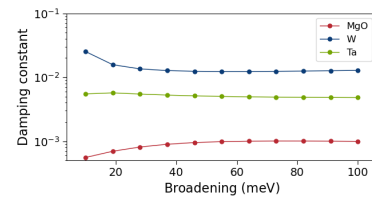

Fig. 5. Gilbert damping as a function of broadening parameters. For all values of the broadening, the W capped structure has a significantly larger damping constant the Ta and MgO structures.

function of the level broadening parameter. Such broadening might be caused by electron-phonon coupling but could in principle also have different contributions. Here we treat it as a free parameter. We observe a very significant modification of the damping constant for the three different capping materials. While the MgO capping results in values of ~ 0.001 in good agreement with previous calculated values for pure Fe, the Ta and in particular the W capping leads greatly increased damping constant of 0.005 and 0.012 with a broadening of 0.1 eV.

V. Discussion

In the sections above we have calculated parameters relevant for reading (TMR), writing (STT, damping), and storage stability (ΔE, T_C). In Fig. 6 (a) we summarize the result by performing a relative comparison of the three capping materials. For each quantity we calculate the relative quantity such that the best capping material is normalized to 1. Since the best damping (α) is the lowest we normalize it as α_{min}/α, whereas for the other quantities we plot A/A_{max}, where A is either Curie temperature, MAE evaluated at 300 K for a 10 nm diameter cylinder, absolute STT averaged at ± 0.5 V, or TMR averaged at ± 0.1 Volt.
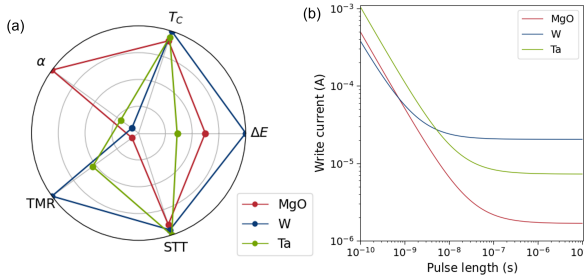

Fig. 6. Relative performance comparison of calculated parameters (a) and write current (b) calculated using (2).

We also estimate the write current required for switching as [20]

$$I_W = \frac{M_S V e}{P g \mu_B} \left[\frac{2}{\tau_D} + \frac{1}{t_p} \ln\left(\frac{\pi^2 \Delta E}{4 P_{BER}} \right) \right]. \qquad (2)$$

where V is the volume of the magnetic material, P the spin polarization factor (here assumed to be proportional to the STT), t_p the pulse length, P_{BER} the bit error rate and $1/\tau_D = \gamma \alpha H_K$ with γ being the gyromagnetic ratio and H_K the anisotropy field. In 6 (b) we plot the write current as a function of pulse length. We use $P_{BER} = 10^{-5}$ and assume $\Delta = 60$. This leads to the different diameters reported above and thus different volumes. In the long pulse length limit, the large damping of the W capping leads to the largest currents. However, for short pulse length $t_p < 1$ nm, the W capped DS-MTJ has the lowest switching current, due to the reduced magnetic moment $M_S V$.

The DFT-calculated parameters presented here are relevant in their own right, but can also be coupled to a TCAD workflow [19] allowing for device-level characterization including new materials and novel MTJ stack designs. This will be a topic of future work.

VI. Conclusion

We have presented a computational study of different capping layer materials (MgO, W, Ta) in double spin-torque MTJ structures. Using fully atomistic calculations based on DFT, we have calculated key parameters relevant for the reading, writing, and storage performance of STT-MRAM devices. W is the best material for both thermal stability, STT, and TMR, and has the lowest write current for short pulse widths. For long pulse

widths, the large Gilbert damping of W is however problematic for reducing the switching current. We emphasize that the methods and analysis tools presented here are not limited to the materials studied here, but are readily available for further studies of different materials for both the magnetic and non-magnetic layers.

References

[1] D. C. Worledge, "Spin-transfer-torque MRAM: the next revolution in memory," in *2022 IEEE International Memory Workshop (IMW)*, 2022, pp. 1–4.

[2] G. Hu *et al.*, "STT-MRAM with double magnetic tunnel junctions," in *2015 IEEE International Electron Devices Meeting (IEDM)*, 2015, pp. 26.3.1–26.3.4.

[3] G. Hu *et al.*, "2x reduction of STT-MRAM switching current using double spin-torque magnetic tunnel junction," in *2021 IEEE International Electron Devices Meeting (IEDM)*, 2021, pp. 2.5.1–2.5.4.

[4] C. Safranski, *et al.*, "Reliable sub-nanosecond MRAM with double spin-torque magnetic tunnel junctions," in *2022 IEEE Symposium on VLSI Technology and Circuits*, 2022, pp. 288–289.

[5] QuantumATK version U-2022.12, Synopsys QuantumATK (https://www.synopsys.com/silicon/quantumatk.html)

[6] S. Smidstrup *et al.*, "QuantumATK: an integrated platform of electronic and atomic-scale modelling tools," *Journal of Physics: Condensed Matter*, vol. 32, no. 1, p. 015901, oct 2019.

[7] A.V. Shapeev, "Moment Tensor Potentials: A Class of Systematically Improvable Interatomic Potentials", *Multiscale Modeling & Simulation*, vol. 14, no. 3, p. 1153, 2016.

[8] B. K. Nikolic *et al.*, *First-Principles Quantum Transport Modeling of Spin-Transfer and Spin-Orbit Torques in Magnetic Multilayers*. Cham: Springer International Publishing, 2018, pp. 1–35.

[9] T. Scheike *et al.*, "Exceeding 400% tunnel magnetoresistance at room temperature in epitaxial Fe/MgO/Fe(001) spin-valve-type magnetic tunnel junctions," *Applied Physics Letters*, vol. 118, no. 4, p. 042411, 2021.

[10] Q. L. Ma *et al.*, "Temperature dependence of resistance in epitaxial Fe/MgO/Fe magnetic tunnel junctions," *Applied Physics Letters*, vol. 95, no. 5, p. 052506, 2009.

[11] M. Zacharias, C. E. Patrick, and F. Giustino, "Stochastic approach to phonon-assisted optical absorption," *Phys. Rev. Lett.*, vol. 115, p. 177401, Oct 2015.

[12] T. Gunst, T. Markussen, M. L. N. Palsgaard, K. Stokbro, and M. Brandbyge, "First-principles electron transport with phonon coupling: Large scale at low cost," *Phys. Rev. B*, vol. 96, p. 161404, Oct 2017.

[13] L. Le Laurent, C. Barreteau, and T. Markussen, "Magnetocrystalline anisotropy of Fe, Co, and Ni slabs from density functional theory and tight-binding models," *Phys. Rev. B*, vol. 100, p. 174426, Nov 2019.

[14] X. He, N. Helbig, M. J. Verstraete, and E. Bousquet, "TB2J: A Python package for computing magnetic interaction parameters," *Computer Physics Communications*, vol. 264, p. 107938, 2021.

[15] R. F. L. Evans *et al.*, "Atomistic spin model simulations of magnetic nanomaterials," *Journal of Physics: Condensed Matter*, vol. 26, no. 10, p. 103202, feb 2014.

[16] P. Asselin *et al.*, "Constrained Monte Carlo method and calculation of the temperature dependence of magnetic anisotropy," *Phys. Rev. B*, vol. 82, p. 054415, Aug 2010.

[17] D. Thonig and J. Henk, "Gilbert damping tensor within the breathing Fermi surface model: anisotropy and non-locality," *New Journal of Physics*, vol. 16, no. 1, p. 013032, jan 2014.

[18] A. V. Khvalkovskiy *et al.*, "Basic principles of STT-MRAM cell operation in memory arrays," *Journal of Physics D: Applied Physics*, vol. 46, no. 7, p. 074001, jan 2013.

[19] H. Dixit *et al.*, "TCAD device technology co-optimization workflow for manufacturable MRAM technology," in *2020 IEEE International Electron Devices Meeting (IEDM)*, 2020, pp. 13.5.1–13.5.4.

[20] L. Thomas *et al.*, "STT-MRAM devices with low damping and moment optimized for LLC applications at Ox nodes," in *2018 IEEE International Electron Devices Meeting (IEDM)*, 2018, pp. 27.3.1–27.3.4.